



# City Research Online

## City St George's, University of London

**Citation:** Lalicata, L. M., Stallebrass, S. E. & McNamara, A. M. (2023). An experimental study into the ultimate capacity of an 'impression' pile in clay. *Geotechnique*, 73(5), pp. 455-466. doi: 10.1680/jgeot.21.00168

This is the accepted version of the paper.

This version of the publication may differ from the final published version. To cite this item please consult the publisher's version.

**Permanent repository link:** <https://openaccess.city.ac.uk/id/eprint/27533/>

**Link to published version:** <https://doi.org/10.1680/jgeot.21.00168>

**Copyright and Reuse:** Copyright and Moral Rights remain with the author(s) and/or copyright holders. Copies of full items can be used for personal research or study, educational, or not-for-profit purposes without prior permission or charge, unless otherwise indicated, provided that the authors, title and full bibliographic details are credited, a hyperlink and/or URL is given for the original metadata page and the content is not changed in any way. For full details of reuse please refer to [City Research Online policy](#).

1 ***An experimental study into the ultimate capacity of an “impression” pile in clay***

2 **Authors:**

3 Leonardo Maria Lalicata, MSc, PhD\*

4 Sarah Elizabeth Stallebrass, MA, PhD\*

5 Andrew McNamara, MSc, PhD\*

6 \* City, University of London, London, England, United Kingdom, EC1V 0HB

7

8 **Corresponding author:**

9 Dr Leonardo Maria Lalicata

10 leonardo.lalicata@city.ac.uk

11

12 **Abstract**

13 The ultimate capacity of a novel type of piled foundation called an “impression” pile has been  
14 investigated using centrifuge modelling techniques. The name derives from the small discrete  
15 impressions created in the side walls of a bored cast in situ pile to increase the soil/pile friction  
16 such that the impressions form nodules on the shaft of the concreted pile. The technology is  
17 suitable for bored piles in overconsolidated clay, such as London Clay. The experiments explored  
18 the influence of geometrical parameters such as the vertical spacing of the impressions, their  
19 number at each level and their shape. The data show a consistent increase in pile capacity of  
20 40% when the impressions extend over 85% of the pile length. The ultimate capacity of the pile  
21 is primarily affected by the length of the pile which is impressed, the number of nodules at a given  
22 cross section and the spacing of the nodules in the vertical direction, as long as this is greater  
23 than a threshold value. According to the experimental evidence, a block failure occurs for a  
24 spacing lower than this threshold value. Plastic failure mechanisms for the impression pile were  
25 established. These were used successfully to calculate the ultimate capacity of the impression  
26 piles tested with an error of less than 10%.

27

28 *Keywords:* impression pile, centrifuge modelling, axial loading, overconsolidated clay, enhanced  
29 capacity

30

31 **List of notations**

32	$A$	cross section of the pile
33	$A_{nod}$	cross section of the nodule
34	$b$	protruded length of the nodule (or rib)
35	$CL$	centre line
36	$CSL$	critical state line
37	$d$	pile diameter
38	$G_s$	Specific gravity
39	$g$	gravity acceleration
40	$h$	height of the nodule (or rib)
41	$L$	pile length
42	$l$	width of the nodule (or rib)
43	$L_a$	active length of the impression pile
44	$n$	number of nodules in the cross section of the pile
45	$M$	Slope of the critical state line in the q-p' plane
46	$N_c$	end bearing factor for the undrained shear strength
47	$N_{c,nod}$	nodule end bearing factor for the undrained shear strength
48	$N_{c,PL}$	rib end bearing factor for the undrained shear strength under plain strain condition
49	$N_{c,rib}$	rib end bearing factor for the undrained shear strength
50	$OCR$	overconsolidation ratio
51	$p'$	mean effective stress
52	$P_{ext}$	circumference of the pile plus rib
53	$P_{pile}$	circumference of the pile
54	$Q, Q_u$	load on the pile, capacity of the pile
55	$Q_b$	base capacity
56	$q_b$	bearing pressure
57	$Q_{b,nod}$	base capacity the nodule
58	$Q_s$	shaft capacity
59	$Q_{s,block}$	shaft capacity between two connecting ribs
60	$Q_{s,in La}$	shaft capacity inside the active length

61	$Q_{s,intra\ nod}$	shaft capacity between the vertical blocks connecting the nodules
62	$Q_{s,nod}$	shaft capacity on the vertical blocks connecting the nodules
63	$Q_{s,out\ La}$	shaft capacity outside the active length
64	$Q_{s,single}$	shaft capacity on two individual ribs
65	$s$	vertical spacing between two horizons of nodules (or ribs)
66	$S_u, S_{u,w}, S_{u,vane}, S_{u(base)}$	undrained shear strength, undrained shear strength from water content,
67		undrained shear strength from hand vane test, undrained shear strength at the pile base
68	$v$	specific volume
69	$W$	dead weight of the pile
70	$w$	gravimetric water content
71	$z$	depth
72	$\Gamma$	specific volume on the CSL at $p'=1$ kPa
73	$\alpha$	soil-pile adhesion factor
74	$\delta$	pile head settlement
75	$\gamma$	unit weight of soil
76	$\lambda$	slope of the normal compression line in the $v-lnp'$ space
77	$\sigma_v$	vertical stress
78	$\xi$	shape factor
79		

80 **Introduction**

81 Very often, the most important factor in determining the ultimate capacity of a pile subjected to  
82 axial load is the shaft resistance. In clays, the maximum shear stress developed on the pile shaft  
83 is often assumed to be a fraction of the undrained shear strength of the soil,  $s_u$ . The adhesion  
84 factor,  $\alpha$ , is an empirical parameter that defines this fraction and accounts for the disturbance  
85 created during the construction of the pile. It depends on the process used in constructing the  
86 pile, the properties of the clay and the site conditions (such as relative humidity and drainage  
87 towards the pile bore). For piles embedded in stiff clays  $\alpha$  can be as low as 0.35 or 0.5, depending  
88 on the construction technology used (Cherubini and Vessia, 2007). It is attractive therefore to  
89 develop a new construction technique that aims to improve the soil-pile interface strength.

90

91 Over the years, many piling contractors have experimented with various methods for enhancing  
92 shaft capacity (Hard and Carvalho, 2018; Karkee *et al.*, 1988; Watanabe *et al.*, 2011; Zhou *et al.*,  
93 2020; Stainer *et al.*, 2011); including the manufacture of special tools to scrape concentric rings  
94 that protrude beyond the nominal pile diameter (Ground Engineering, 2003; Hard and Carvalho,  
95 2018). This produces a ribbed profile along the shaft which has the effect, in an ultimate capacity  
96 test, of creating a failure surface between the ribs where there is a soil-soil interface. However,  
97 owing to the obvious commercial benefits that might accrue from such a development, there is  
98 very little published material relating to pile shaft modification. Ground Engineering (2003)  
99 described some field trials on ribbed piles. The ribs were found to enhance the ultimate capacity  
100 of 750mm diameter piles, constructed in glacial clay, by as much as 30%. Gorasia and McNamara  
101 (2016) presented the results of a series of centrifuge tests on ribbed piles demonstrating that the  
102 capacity increase could reach 40% for a pile 800mm in diameter with ribs protruding by 75mm (at  
103 prototype scale). Small scale tests by Qian *et al.* (2016) demonstrated that the pull-out capacity  
104 of a ribbed helical pile in sand, 50mm in diameter and with rib length of 8 mm, may be up to 5  
105 times higher than that of a straight plain pile. The authors found that the capacity increase  
106 depended on the rib spacing,  $s$ , and that the maximum capacity occurs at an  $s/d$  ratio of  
107 approximately 1, where  $d$  is the diameter of the pile (without ribs). Similar conclusions were found  
108 by Merifield (2011),  $s/d=1.58$ , and Rao *et al.* (1991),  $s/d=1.0 - 1.5$ , studying the uplift capacity of  
109 helical anchor plates in clay, where  $d$ , in this case, is the diameter of the plate. The slight increase

110 in critical spacing is probably due to the different failure mechanism for these anchor plates. Both  
111 Gorasia and McNamara (2016) and Qian *et al.* (2016) found that ribbed piles have a higher  
112 capacity than straight piles with a diameter equal to the outer diameter of the ribbed pile.

113

114 A major issue associated with ribbed piles is the removal of spoil from the bore prior to concreting.  
115 To address this, an alternative method of increasing pile/soil interface roughness is to profile the  
116 shaft walls by creating small impressions that lead to a nodular pile surface; this avoids the  
117 generation of any loose spoil. A special tool has been developed by Keltbray Piling (Patent no:  
118 P027299GB/JMF/ZJH) to undertake this profiling, at prototype scale, and create what has been  
119 termed an “impression pile”. It is this form of pile shaft friction improvement that is the focus of  
120 this research project. A conceptual sketch of the impression pile is shown in Figure 1, together  
121 with the ribbed pile reported for comparison purposes. In the simplest configuration, four nodules  
122 are impressed at a given cross section, spaced at 90° around the axis of the pile, and nodules  
123 are aligned in the vertical direction, although other configurations may be used.

124 Following the successful proof of concept, (Lalicata *et al.*, 2020), a large parametric study in the  
125 geotechnical centrifuge has been carried out to explore the influence of impressions on the  
126 ultimate capacity of a pile. The results are described in this paper. A possible failure mechanism  
127 is developed to explain the results obtained. The equipment developed for model pile testing was  
128 designed to be flexible in order to permit testing of a wide range of possible impression  
129 configurations.

130

## 131 **1. Experimental work**

### 132 **1.1. Methodology**

133 The enhanced ultimate capacity of impression piles subjected to a static vertical force was  
134 explored in centrifuge tests undertaken at 50g using a homogeneous overconsolidated clay  
135 deposit. In each experiment, the impression piles were tested alongside a plain, straight shafted  
136 pile to provide a baseline response for comparison purposes.

137

138 The Geotechnical Engineering Research Group at City, University of London, makes use of an  
139 Acutronic 661 beam centrifuge, described in detail by Schofield and Taylor (1988) and McNamara

140 *et al.* (2009). The package containing the model was installed on the centrifuge once the piles  
141 had been bored, impressed and cast and the loading apparatus assembled on the plane strain  
142 strongbox. The whole process took approximately 2 hours.

143

144 During the centrifuge tests, the water table was maintained at a depth of approximately 10mm  
145 below ground level by means of a constant head standpipe connected to the bottom of the model.  
146 The top surface was sealed with a sprayed synthetic rubber coating to prevent clay drying during  
147 the test, once dried this was only ~400  $\mu\text{m}$  thick and it is known to not influence soil settlements  
148 (Le, 2017). The sample was allowed to come into pore pressure equilibrium and the piles were  
149 then loaded until failure at a displacement rate of 1mm/min.

150

### 151 **1.2. The experimental arrangement**

152 For each test, the soil sample provided up to four testing sites within the rectangular strongbox,  
153 Figure 2. The piles were positioned on the centreline of the model, 100 mm from the sides, which  
154 was far enough to minimise boundary effects (Phillips, 1995).

155

156 The piles, were spaced 110 mm apart and loaded simultaneously by means of a very stiff beam  
157 connected to a lead screw and motor. The apparatus was devised so that it was possible to obtain  
158 independent load and settlement data for each pile. Experimental evidence collected over the  
159 years suggest that the capacity of a pile is not affected by neighbouring piles when they are  
160 spaced more than 2-3.5d (De Mello, 1969; O'Neill *et al.*, 1982; Cooke, 1986; Conte *et al.*, 2003;  
161 Mandolini *et al.*, 2005; De Santis and Mandolini, 2006). Therefore, the pile spacing adopted in  
162 this study, 6.9d, is sufficient. This necessitated the development of several novel components.  
163 These included a loading system and independent measurement of pile displacement together  
164 with the guides, jigs and impression tools needed to create the model piles. The details of these  
165 are given in Lalicata *et al.* (2020).

166

### 167 **1.3. "Impression pile"**

168 The test piles were 16mm in diameter and 180 mm long, replicating a prototype pile 800mm  
169 in diameter by 9m long. The pile length to diameter ratio of 11.25 is small if compared to typical

170 piles used in the field, which can be up to 50, but a reasonable compromise given the need to  
171 provide sufficient soil under the base of the piles and the limited depth of clay available. The  
172 nodules on the model test piles protruded from the shaft by  $1.5\text{mm} \pm 0.05\text{mm}$  and were  $3\text{mm}$   
173  $\pm 0.05\text{mm}$  wide, as measured post-test. As shown in Figure 3, two different nodule shapes were  
174 tested. The first had a circular cross section and a domed head, whilst the second had a square  
175 side with a flat pyramidal tip. The shapes had the same maximum protruded length and cross-  
176 sectional dimension (diameter = square side =  $3\text{mm}$ ).

177

178 The piles were excavated using a  $16\text{mm}$  diameter thin walled stainless-steel tube guided by a  
179 collar to guarantee verticality. An innovative impression tool was developed to form the nodules.  
180 It was designed to be smaller than the bore diameter when closed and to form the impressions  
181 when open, Lalicata *et al.* (2020). For a given depth the tool impressed two nodules at a time,  
182 and was then rotated by  $90$  degrees for the second pair of nodules along an orthogonal axis. A  
183 sketch of the vertical cross section of the impression tool and the guide system is shown in Figure  
184 4.

185

186 Once the impressions were completed, the piles were cast using a polyurethane fast cast resin,  
187 Sika Biresin G27 (McNamara, 2001; McNamara and Taylor, 2002; Gorasia and McNamara,  
188 2016). Aluminium powder was used as filler to increase the weight of the pile. The mixture was  
189 designed to have a good fluidity to fill the impressions. The resulting pile density was  $1.45\text{ g/cm}^3$ ,  
190 the components placed on the pile head to accommodate the loading and measurement  
191 equipment provided an additional dead weight of  $13.4\text{N}$  or  $21.6\text{N}$  (at  $50\text{g}$ ) depending on the type  
192 of instrumentation installed, Lalicata *et al.* (2020). Uniaxial compression tests were undertaken  
193 to measure the mechanical properties of the resin when set. The resin was found to have a  
194 Young's Modulus equal to  $1.1\text{GPa}$  and a yield stress of  $35\text{MPa}$ . These values confirm that the  
195 pile behaves as a linear elastic material in the range of the applied loads.

196

197 **1.4. Soil**

198 The Speswhite Kaolin clay used in the tests was prepared from slurry with an initial water content  
199 of approximately 120%; which is twice the liquid limit. The slurry was created by mixing dry powder  
200 and distilled water in an industrial ribbon blade mixer.

201 The slurry was carefully placed into the model container and manually agitated to expel the main  
202 air bubbles. The inside faces of the model container had been previously coated with water pump  
203 grease to minimise friction at the boundaries (Philipps, 1995). Beneath the slurry there was a filter  
204 paper and a 3 mm porous plastic sheet, with an aluminium drainage plate at the base. On top of  
205 the slurry, a second filter paper and porous plastic sheet were placed and drainage was allowed  
206 through holes in a loading platen. Consolidation was achieved by means of a hydraulic press over  
207 a period of 9 days including 1 day of swelling. The samples were compressed to a vertical stress  
208 of 500kPa that was then reduced to 250kPa, producing a firm, but still workable, clay sample  
209 (McNamara *et al.*, 2009; Taylor *et al.*, 2012; Divall and Goodey, 2015; Gorasia and McNamara,  
210 2016).

211

212 Following testing on the centrifuge, the undrained shear strength was estimated from hand vane  
213 tests and water content samples. The water content of samples taken from the model, Figure 5  
214 (a), were converted to soil strengths using eq. (1) (Wood, 2004) and values of relevant parameters  
215 published by Stallebrass and Taylor (1997) with a small adjustment to the value of the specific  
216 volume on the critical state line at a mean effective stress of 1kPa,  $I$ . This was changed from  
217 2.997 to 3.04 in order to obtain values of strength consistent with those from the hand shear vane.  
218 The values of the parameters and their meaning are listed in Table 1.

$$s_u = \frac{1}{2} M e^{\frac{(I-v)}{\lambda}} \quad (1)$$

219 where  $v$  is the specific volume.

220

221 Soil strength measurements for the tests are given in Figure 5 (b) and (c) respectively for the  
222 values derived from water contents  $s_{u,w}$  and for those derived from hand vane tests  $s_{u,vane}$ . The  
223 measurements are largely consistent across all tests and, in both cases, the data are generally  
224 inside the 10% error band with respect to the best fit line. As might be expected, the undrained

225 strength increased slightly with depth as water content reduced. The manufacturer of the hand  
226 vane (Pilcon, 2020) notes that this should be used for generic in-situ indications only,  
227 consequently water content measurements were used to give a more precise indication of the  
228 variation in undrained strength for the purposes of normalising the data and a best fit to these  
229 data is as follows:

230

$$s_{u,w} = 41.2 + 0.044z \quad (2)$$

231

232 where  $s_{u,w}$  is expressed in kPa and  $z$  in mm.

233 The profile of the overconsolidation ratio,  $OCR$ , with depth for the tests is reported in Figure 5 (d).

234

## 235 **2. Results**

### 236 **2.1. Parameters investigated**

237 The results of the experimental parametric study are presented in this section. The detail of the  
238 nodule dimensions and the main features of the impression pile are shown in Figure 1. The  
239 parameters varied were:

- 240 • The active length,  $L_a$ : the portion of the pile shaft where the impressions were created;
- 241 • The spacing,  $s$ : the vertical distance between two levels of nodules
- 242 • The number of nodules at a given cross section,  $n$ ;
- 243 • The position of the centre of the impressed zone relative to the soil surface,  $z$ .

244 The length parameters listed above have all been made non-dimensional as listed in Table 2,  
245 which also gives the range of values investigated.

246

### 247 **2.2. Experimental variability**

248 The behaviour of the piles has been characterised using their load deflection response. The  
249 ultimate compressive capacity  $Q_u$  is the asymptotic value of the curve after the peak where the  
250 shaft and the base resistance may be assumed fully mobilised. In the model tests, the ultimate  
251 capacity of the plain piles ranged between 342N and 430N (model scale), Table 3.

252

253 The head displacement was not always sufficient to reach a fully flattened plateau; therefore, the  
 254 ultimate capacity recorded has, in some tests, been estimated, Figure 6. However, because the  
 255 increase or decrease in capacity post peak does not vary significantly with settlement the  
 256 maximum uncertainty in these values is 10N. For each test,  $\alpha$  was back calculated from  $Q_u$  taking  
 257 into account the dead weight of the pile, assuming the base resistance was fully mobilised and  
 258 adopting the  $s_{u,w}$  distribution measured in the relevant test. Where the values of ultimate load are  
 259 estimated, the value of  $\alpha$  given varies by up to 0.03.

260 Following Skempton (1951), the base resistance is expressed as:

$$Q_b = A \cdot q_b = \pi \frac{d^2}{4} \cdot (N_c \cdot s_{u(base)} + \sigma_v) \quad (3)$$

261  
 262 Where  $A$  is the cross-sectional area of the pile base,  $N_c$  is the bearing factor, taken as equal to 9,  
 263 (Meyerhof, 1951; Martin and Randolph, 2001; Khatri and Kumar, 2009) related to the soil strength  
 264  $s_u$  and  $\sigma_v = \gamma \cdot L$  which is the overburden pressure at the base of the pile.

265  
 266 The variation in ultimate capacity from 342N to 430N is significant, but well correlated with the  
 267 undrained shear strength,  $s_{u,w}$  evaluated at  $z=L/2=90\text{mm}$ , Figure 7. In the plot, the grey symbols  
 268 represent the data where the load settlement curve did not reach a constant value and ultimate  
 269 capacities have been estimated. The theoretical capacity of the pile is calculated as the sum of  
 270 the load taken in skin friction along the shaft,  $Q_s$ , and the load provided by the end bearing,  $Q_b$ ,  
 271 minus the self-weight,  $W$ :

$$Q_u = Q_b + Q_s - W \quad (4)$$

272  
 273 The  $s_u$  distribution adopted is given by Eq. (2) and an adhesion factor,  $\alpha$ , equal to 0.73. This is  
 274 the average back calculated value reported in Table 3. A good correspondence between the  
 275 theoretical ultimate load and the experimental results is apparent considering the variability of  $s_{u,w}$   
 276 (see Figure 5 (b)).

277

278 **2.3. Ultimate capacity of the impression pile**

279 The ultimate capacities of the impression piles are listed in Table 4 together with the main  
280 parameters describing the patterns of nodules on the pile shafts, such as the shape and the  
281 number of nodules, the active length, the spacing and position of the impression zone along the  
282 pile. The nodules protruded from the shaft by 1.5mm and were 3mm wide. If there was insufficient  
283 settlement for the ultimate load to be reached this has been estimated following the same  
284 approach as was used with the plain piles and with the same maximum uncertainty of 10N.  
285 Differences in the load settlement response at large displacement, with respect to the plain piles,  
286 are reported and discussed in Lalicata *et al.* (2020).

287

288 The influence of the impression variables on the ultimate capacity of the piles is plotted in Figures  
289 8-11. In each figure, plot (a) gives the ultimate capacity presented as a function of the physical  
290 variable, described in Table 4, while plot (b) gives the increase in capacity plotted against the  
291 normalised variable. The increase in capacity is the ratio of the ultimate capacity of the impression  
292 pile and the plain pile evaluated for each test. Theoretically, this procedure should account for  
293 any small variation in soil properties between the different tests. In practice, marginal differences  
294 in the ultimate capacity of both the impression and the plain pile may result in a small, but not  
295 negligible variation in the increase in capacity equal to a maximum of  $\pm 5\%$ . In all the plots the  
296 pyramidal nodules are pictured as open square symbols and the domed nodules are open circles.  
297 The grey symbols represent data from the tests where the ultimate capacity was an estimate  
298 because there was insufficient settlement to reach this state and the diamonds represent the piles  
299 where the spacing of the pyramidal nodules was very high (60mm and 120mm). To allow  
300 comparisons to be made, data from the tests in Table 4 have been selected so that only one  
301 parameter is changed in each plot while the others are maintained constant.

302

303 The influence of the active length  $L_a$  is clearly presented in Figure 8 which shows both the ultimate  
304 load and the proportional change in capacity increase with  $L_a$ . Both of the plots indicate that the  
305 shape of the nodules, owing to the small dimensions of the impression, only marginally influence  
306 the ultimate capacity of the piles. For comparison, the ultimate capacity of a plain pile is presented  
307 in Figure 8 (a) showing that, for constant  $L_a$ , the variability of the impression pile results is similar

308 or lower than that observed for the plain piles and discussed in the previous section. The  
309 effectiveness of the nodules increases with  $L_a$ , and when this is  $\sim 0.85L$ , the increase in capacity  
310 is approximately 40%.

311 Figure 9 presents the influence of the spacing,  $s$ , between nodules. When  $s$  increases from 30mm  
312 to 60mm the ultimate capacity drops significantly (Figure 9 (a)). For  $s < 30$ mm the pile response is  
313 similar allowing for experimental variability. This appears to be because the failure surface around  
314 the nodules bridges vertically creating a vertical block of soil connecting adjacent nodules with  
315 the failure surface on the outside of this block. This is supported by inspection of the exhumed  
316 piles at the end of the tests. For high spacing, this does not occur and failure takes place by soil  
317 flowing around individual nodules. Qualitatively, the normalised plot in Figure 9 (b) shows the  
318 same result although the data could be interpreted to show a higher critical spacing. The average  
319 increase in capacity is  $\sim 25\%$  for the block case, reducing to 12% for the highest spacing of  
320 120mm.

321

322 Ultimate capacity increases with the number of nodules  $n$ , Figure 10 (a). The increase in capacity,  
323 Figure 10 (b), increases linearly with the number of nodules and for  $n=4$ , all but one set of data  
324 are consistent. Inspection of Figure 11 (a) seems to indicate that the position of the impressions  
325  $z$  has a minor influence on the pile capacity. In both Figures 10 and 11 there is an increased  
326 scatter when the data are presented as increase in capacity, which was not expected as this  
327 should remove any variability associated with variations in undrained strength.

328

### 329 **3. Back Analysis of Impression Pile Ultimate Capacity**

330 The results from the centrifuge tests illustrate the main parameters affecting the ultimate capacity  
331 of the impression pile.

- 332 • The increase in capacity of the impression pile is approximately constant if the vertical  
333 spacing is lower than a threshold value,  $s/b$  between 20 and 40, Figure 9. It is  
334 assumed that within this threshold, no relative displacement occurs between the shaft  
335 of the pile and the soil between the nodules and the failure surface is on the outside  
336 of the nodules that are connected in the vertical direction, Figure 12. When the  
337 vertical spacing increases beyond this threshold value, the nodules behave as

338 individual embedded foundations. As the number of nodules reduces in a given active  
339 length, the increase in capacity of the impression pile reduces as well.

- 340 • Below the threshold spacing, the increase in capacity appears to be a linear function  
341 of the number of nodules in the pile cross section; at least for the range explored (see  
342 Figure 10). This suggests that the nodules connect in the vertical direction only;  
343 forming independent vertical blocks of similar cross-sectional dimensions. A limiting  
344 number of nodules will certainly exist, but the data collected in this study do not allow  
345 conclusive statements to be made.
- 346 • The increase in capacity of the piles is proportional to the length of pile impressed  
347 with nodules if the nodules are less than the critical spacing apart.
- 348 • The vertical position of the nodules has little effect on pile capacity for the soil  
349 conditions studied,  $s_u$  only increasing marginally with depth, and the pile geometry  
350 tested.

351

352 Given the above, the ultimate capacity of the impression pile is calculated by extending design  
353 methods for a plain pile and is illustrated in Figure 12 for the block mechanism. The base capacity  
354  $Q_b$  remains the same as the straight pile. The shaft capacity  $Q_s$  is divided in two parts: one inside  
355 the active length  $L_a$ ,  $Q_{s,in L_a}$  and the other outside the active length,  $Q_{s,out L_a}$ . Inside the active length  
356 the shaft resistance develops in a different manner with respect to the nodules,  $Q_{s,nod}$ , and the  
357 pile shaft,  $Q_{s,intra nod}$ . Finally, an additional contribution is provided by the bearing capacity of the  
358 nodule  $Q_{b,nod}$  that is included only once, for the lowest nodules in the group. For simplicity it is  
359 assumed that the failure surface in the horizontal plane has the same cross-sectional dimensions  
360 as the nodule.

361

362 The base resistance is calculated with eq. (3). Outside the impressed zone the skin friction is the  
363 same as the plain pile:

$$Q_{s,out L_a} = \pi d \cdot \alpha s_u (L - L_a) \quad (5)$$

364

365 Inside the active length the two contributions are:

$$Q_{s,nod} = n \cdot 4b \cdot s_u \cdot L_a \quad (6)$$

366

$$Q_{s,intra\ nod} = (\pi d - 2b \cdot n) \cdot \alpha s_u \cdot L_a \quad (7)$$

367

368 In the block, it is assumed for simplicity that the failure occurs in the soil only, where the adhesion  
 369 factor is taken as equal to one. Due to the small dimensions of the nodules, eq. (6) neglects the  
 370 reduction in  $\alpha$  at the nodule/soil interface. For constant  $\alpha$  values, the accuracy of this assumption  
 371 increases as the spacing increases. Between two blocks, failure takes place on the shaft of the  
 372 pile, where  $\alpha$  is assumed to be the value back calculated from the plain pile test.

373

374 When the spacing between the nodules is higher they behave as individual embedded  
 375 foundations, such that  $L_a=0$  and  $Q_{s,nod} = Q_{s,intra\ nod} = 0$  and  $Q_{b,nod}$  must be evaluated for each nodule  
 376 horizon .

377 The end bearing of the nodules is:

$$Q_{b,nod} = n \cdot A_{nod} (N_{c,nod} s_u + \sigma_v) \quad (8)$$

378

379 Where  $A_{nod}$  is the cross-sectional area of the nodule; equal to  $2b^2$  in this case. The bearing factor  
 380  $N_{c,nod}$  is calculated using an upper bound solution presented in the next section.

381

### 382 3.1.1. End bearing of the single nodule

383 The failure mechanism around a single nodule is three-dimensional, thus 3D conditions should  
 384 be considered. However, as a first approximation, the end bearing of a nodule can be assumed  
 385 to be similar to that of a section of a rib and the rib can be studied under axisymmetric conditions.  
 386 Thus, the spread of the failure mechanism around a single nodule in the horizontal direction is  
 387 not considered for simplicity and consistency with the lateral extent of the block mechanism  
 388 described above. The bearing factor for the rib,  $N_{c,rib}$ , is derived using upper bound theorems of  
 389 plastic collapse for a rigid perfectly plastic weightless material with a Tresca failure criterion. The  
 390 adhesion factor on the soil-rib interface,  $\alpha$ , is varied from 0 (smooth) to 1.0 (rough). The  
 391 mechanism is similar to that of a deep buried anchor plate (Merifield and Smith, 2010; Merifield,

392 2011; Martin and Randolph, 2001) although in this case the presence of the pile shaft cannot be  
393 neglected.

394

395 The assumed failure mechanism and the associated hodograph are presented in Figure 13: below  
396 the rib, there is an annular wedge of soil attached to the rib that slides along a surface inclined at  
397 45° to the horizontal. Beside the wedge, a fan zone with internal angle  $3/4\pi$ , guarantees kinematic  
398 compatibility and finally another block of soil, the same height as the rib, rises as the rib descends.

399

400 The expression for the bearing factor of the single rib is thus:

$$N_{c,nod} = N_{c,rib} = \xi \left( (2 + 3\pi) + (\sqrt{2} + (2 + \sqrt{2}) \cdot \alpha) \right) \quad (9)$$

401

402 Where  $\xi$  is a shape factor accounting for the axisymmetric conditions, it decreases with  
403 decreasing  $b/d$  ratio and is practically independent from  $\alpha$ . Here  $\xi$  is equal to 1.097. Further details  
404 on the  $N_{c,rib}$  and  $\xi$  derivation are given in the Appendix A.  $N_{c,rib}$  is equal to 14.11 for  $\alpha=0$  and to  
405 17.81 for  $\alpha=1$ .

406

### 407 3.1.2. Critical vertical spacing

408 The experimental data showed that the impression piles perform best when the nodules form a  
409 block in the vertical direction, when the bearing factor of the single nodule is relatively insignificant  
410 in determining the behaviour of the impression pile. Consequently, understanding when the  
411 nodules behave as a block or independently in the vertical direction is crucial for the design of the  
412 impression pile. The experimental results in Figure 9 suggest that this critical spacing may range  
413 between  $20b$  and  $40b$ . Using the bearing factor in eq. (9) it is possible to express the critical  
414 spacing as a function of the geometry of the impression and the pile and of the adhesion factor.

415 The critical vertical spacing is estimated by comparing the load capacity resulting from two  
416 independent ribs and the shaft capacity developed between them; with the load capacity resulting  
417 from the block failure connecting the two ribs.

418 If the circumference of the pile plus rib is  $P_{ext} = 2\pi \cdot \left( \frac{d}{2} + b \right)$  and the circumference of the pile is

419  $P_{pile} = \pi d$ , the critical vertical spacing when  $Q_s$  is equal for both mechanisms, is given by:

420

$$\begin{aligned}
 Q_{s,block} &= P_{ext} \cdot [s_u \cdot (s - 2b) + \alpha s_u \cdot 2b] \\
 &= \\
 Q_{s,single} &= A_{rib} \cdot N_{c,rib} \cdot s_u + P_{pile} \cdot \alpha s_u \cdot 2b
 \end{aligned} \tag{10}$$

↓

$$\frac{s}{b} = \frac{1}{(P_{ext} - \alpha P_{pile})} \cdot \left[ \frac{A_{rib}}{b} N_{c,rib} - 4\alpha \cdot P_{pile} + 2P_{ext}(1 - \alpha) \right]$$

421

422 Eq. (10) is presented as a function of  $\alpha$  in Figure 14, which shows that the normalised critical  
 423 spacing,  $s/b$ , increases sharply from  $\alpha=0.8$  to 1. This indicates that when the value of shear  
 424 strength of the soil-pile interface approaches that of the soil, the block mechanism prevails;  
 425 whatever spacing is used. Eq. (10) represents an “envelope” above which single nodule behaviour  
 426 is predicted to dominate and below which the block mechanism is predicted. For  $\alpha$  values between  
 427 0.6 and 0.8, as in the centrifuge tests, the  $s/b$  ratio varies from 27.9 to 41.2 which is consistent  
 428 with the experimental results.

429

430

### 431 **3.2. Comparison with experimental data**

432 In the previous section, the expressions for the bearing factor and the critical vertical spacing of  
 433 the nodules were derived for the simplified case of axisymmetric conditions (ribbed pile).  
 434 However, as noted these expressions can also be used to interpret the data from the impression  
 435 piles. In the series of tests undertaken, a block mechanism in the vertical direction occurs except  
 436 for T12 where piles were tested with  $s/b$  equal to 40 and 80. If it is assumed that the nodules do  
 437 not interact in the horizontal direction, which is consistent with the linear increase in  $Q_u$  with  
 438 number of nodules at a given horizon, the ultimate capacity can be computed by considering the  
 439 capacity provided by a series of vertical ribs coincident with the nodules as shown in Figure 12.  
 440 For each prediction, the value of adhesion and the shear strength distribution used to predict the  
 441 load capacity are those measured in the relevant test.

442

443 In Figure 15, the sum of the measured load and the dead weight of the pile is compared with the  
444 predicted net load ( $Q_s+Q_b$ ), calculated using equations (3) to (8). The comparison shows  
445 compatibility between both the block and the independent nodule tests, as all of the predictions  
446 lie inside a 10% error band. The predicted capacities tend, on average, to slightly underestimate  
447 the measured capacities.

448

449 This gives clear evidence that, for the range of geometries tested in overconsolidated clay, the  
450 method set out above is an effective means of undertaking a theoretical calculation of the ultimate  
451 capacity of an impression pile. It can be demonstrated that, due to the small dimensions of the  
452 nodules, the end bearing contribution of the lowermost level of nodules,  $Q_{b,nod}$ , is very small  
453 compared to their contribution in creating the block mechanism. For instance, when  $n=4$  it is  
454 approximately 3.0% of the total ultimate capacity. Therefore, the use of the simplified  
455 axisymmetric analysis for the study of the bearing factor, eq. (9), appears more than justified.

456

## 457 **Conclusions**

458 The paper presents the results of an investigation into the enhanced pile capacity of impressed  
459 piles with an improved soil/pile shaft interface created using a method developed by Keltbray  
460 Piling. The concept consists of profiling the shaft walls by creating impressions that form nodules  
461 projecting into the soil when the pile is concreted leading to an increased soil-pile roughness and  
462 moving the failure surface away from the shaft into the soil. An extensive parametric study was  
463 carried out in a series of geotechnical centrifuge model experiments. The tests modelled bored  
464 piles in overconsolidated clay. In each test the impression piles were tested together with one  
465 plain pile against which the impression piles could be assessed.

466

467 As with all modelling techniques, centrifuge modelling has some level of idealisation which may  
468 not be completely representative of prototype situations. In the tests, installation effects are  
469 neglected as the piles were installed at 1g rather than in the high-g environment. This is clearly  
470 not representative of the prototype scale installation but may be considered as an ideal wished in  
471 place installation of the pile. The resin used to cast the piles was also an idealisation since the  
472 adhesion between the resin and Speswhite kaolin clay sample may not be representative of the

473 adhesion between concrete and a heavily overconsolidated clay. However, both these  
474 idealisations lead to results that would be conservative with respect to an equivalent pile in the  
475 field, i.e. the beneficial effects of the impression piles would be enhanced as the shaft resistance  
476 of the plain concrete piles in the field would be lower owing to the lower soil to pile adhesion  
477 relative to the model piles.

478

479 The main outcomes of this study may be summarised as follows:

- 480 • The increase in capacity of the impression piles depends on the proportion of the pile  
481 impressed, which has been termed the active length,  $L_a$ . When  $L_a \sim 0.85L$ , the increase in  
482 capacity reaches 40%. Therefore, an impression pile having the same capacity as the  
483 plain pile could be reduced in dimensions by  $\sim 37\%$  in length or  $\sim 25\%$  in diameter;
- 484 • There exists a critical vertical spacing, of between  $20b$  and  $40b$ , for the nodules at which  
485 the failure mechanism of the pile changes. If the spacing is lower than the critical  
486 threshold, the failure surface connects the nodules along a vertical alignment. When the  
487 vertical spacing is greater than the critical value the failure occurs around each nodule  
488 independently of surrounding nodules;
- 489 • The relative increase in bearing capacity increases approximately linearly with the  
490 number of nodules at a given cross section. This is because, in the range explored, the  
491 failure surface around the nodules connects in the vertical direction only and not in the  
492 horizontal plane. There will be a limit to the number of nodules for which this is true,  
493 however, the data collected do not allow this limit to be clearly defined.

494

495 A method for the calculation of the ultimate capacity of the impression pile was established using  
496 an upper bound solution under axisymmetric conditions. Although this is technically incorrect, as  
497 the nodule failure is three-dimensional, some findings are still valid especially those in the  
498 (vertical) plane of the application of the load. The upper bound solution provides an expression  
499 for the bearing capacity of the single nodule and an expression for the vertical critical spacing that  
500 depends on geometric variables and on  $\alpha$ . The critical spacing is in good agreement with the  
501 experimental results and it is a key element in the design of these foundations.

502

503 The calculation method considers explicitly the contribution provided by the shear stress  
504 developed along the vertical blocks of soil between the nodules, the skin friction on the remainder  
505 of the shaft and the end bearing of the blocks. The predictions are in extremely good agreement  
506 with the experimental data with a discrepancy of less than 10%. The calculation method detailed  
507 in this paper has been used to define the design method for the impression pile presented in  
508 Lalicata *et al.* (2021).

509

510 The study has demonstrated the benefit to be gained in pile capacity by profiling the shaft of bored  
511 cast in situ piles in clays. The increase in capacity of the impression pile is very promising and  
512 the technology used has the potential to minimise uncertainties in shaft capacity for these  
513 commonly used piles at prototype scale because the pile capacity relies less on the pile adhesion  
514 factor. The analysis method developed explains the main features of the results based on an  
515 appreciation of the mechanisms by which the piles fail and will be a useful tool for designers.  
516 Further work is currently being undertaken to explore the link between the ultimate capacity of the  
517 piles and the performance at working loads.

518

#### 519 **Acknowledgements**

520 This research project would not have been developed without funding from Innovate UK and the  
521 vision of Keltbray Piling. They are gratefully acknowledged. The authors also want to thank  
522 technical staff from City, University of London for their support in the manufacture of all the  
523 components of the experimental set-up. Finally, we would like to thank Professor Neil Taylor and  
524 Professor Michael Davies for their suggestions; Dr Richard Goodey, Dr Sam Divall and all the  
525 geotechnical research group for sharing knowledge and stimulating discussion.

526

#### 527 **References**

- 528 Cherubini C. & Vessia G. (2007). Reliability approach for the side resistance of piles by means of  
529 the total stress analysis ( $\alpha$  method). *Canadian Geotechnical Journal*, **44**, No. 11, 1378–1390.
- 530 Conte G., Mandolini A., and Randolph M. F. (2003). Centrifuge modeling to investigate the  
531 performance of piled rafts. *Proc. Geotech. Int. Seminar on Deep Foundations on Bored and Auger*  
532 *Piles*, Van Impe and Haegeman, eds., 379–386.
- 533 Cooke R.W., Price G. and Tarr K. (1980). Jacked piles in London clay: Interaction and group  
534 behaviour under working conditions. *Géotechnique*, **30**, No.2, 97–136.

- 535 De Mello V.F.B. (1969). Foundations of buildings on clay. State-of the- Art Report, *Proc. VII*  
536 *ICSMFE*, Vol. 1, 49–136.
- 537 de Sanctis L and Mandolini A. (2006). Bearing capacity of piled rafts on soft clay soils. *J. Geotech*  
538 *Geoenviron Eng.* 132, No. 12, 1600–1610.
- 539 Divall S., and Goodey R.J. (2015). Twin-tunnelling induced ground movements in clay.  
540 *Proceedings of the Institution of Civil Engineers: Geotechnical Engineering*, **168**, No.3, 247–256.
- 541 Gorasia, R. J. & McNamara, A. M. (2016). High-capacity ribbed pile foundations. *Proceedings of*  
542 *the Institution of Civil Engineers: Geotechnical Engineering*, **169**, No. 3, 264–275.
- 543 Ground Engineering (2003). Getting to grips with friction. *Ground Engineering, Magazine of the*  
544 *British Geotechnical Association* **26**, 20–21.
- 545 Hard D.A. and Carvalho A.T. (2018). Threaded rotary bored piles at Paddington new yard.  
546 *Proceeding of the 2018 DFI-EFFC International Conference on Deep Foundations and Ground*  
547 *Improvement*, Rome, Italy.
- 548 Karkee M.B., Kanai S. and Horiguchi T., (1998). Quality Assurance in Bored PHC Nodular Piles  
549 Through Control of Design Capacity Based on Loading Test Data. *Proceedings of the 7<sup>th</sup>*  
550 *International Conference and Exhibition, Piling and Deep Foundations*, Vienna, Austria, **1(24):1-**  
551 **9**.
- 552 Khatri V. N. and Kumar J. (2009). Bearing capacity factor  $N_c$  under  $\phi=0$  condition for piles in  
553 clays. *Int. J. of Numerical and Analytical Methods in Geomechanics*; **33**, No 9, 1203–1225.
- 554 Lalicata L. M., McNamara A. M. and Stallebrass S. E. (2020). Experimental technique for creating  
555 enhanced capacity piles in a centrifuge environment. *Proc. of European Conf on Physical*  
556 *Modelling in Geotechnics ECPMG2020, Lulea*, 49-55.
- 557 Lalicata, L.M., McNamara, A. M. and Stallebrass, S. E. (2021). Design method for the “impression  
558 pile”. *Institution of Civil Engineers: Geotechnical Engineering*.  
559 <https://doi.org/10.1680/jgeen.21.00033>.
- 560 Lalicata L.M., McNamara A.M., Stallebrass S.E. and Panchal J.P. (2021). Physical Modelling of  
561 High-Capacity Piles under Axial Loading. *Proc of the Piling 2020 Conference*. 259-264. ICE  
562 Publishing. <https://doi.org/10.1680/pttc.65048.259>
- 563 Mandolini A. (1999). Small-strain soil stiffness and settlement prediction for piled foundations.  
564 *Proc. ff the 2<sup>nd</sup> Int. Symposium on Pre-failure Deformation Characteristics of Geomaterials*, Turin,  
565 Italy. 1397–1404.
- 566 Mandolini A., Russo G. and Viggiani C. (2005). Piled foundations: Experimental investigations,  
567 analysis and design. State-of-the-Art Report. *Proc. of the 16<sup>th</sup> ICSMGE*, Osaka, Japan, Vol. 1,  
568 177-213.
- 569 Martin C. M. and Randolph M. F. (2001). Applications of the lower and upper bound theorems of  
570 plasticity to collapse of circular foundations. *Proc. of 10<sup>th</sup> Int. Conf. on Computer Methods and*  
571 *Advances in Geomechanics, Cairns*, 2; 1417–1428.
- 572 McNamara A.M. (2001). Influence of Heave Reducing Piles on Ground Movements Around  
573 Excavations. *PhD thesis*, City University, London, UK.
- 574 McNamara A.M. and Taylor R.N. (2002). Use of heave reducing piles to control ground  
575 movements around excavations. *Proc. Int. Conf. Physical Modelling in Geotechnics*, St' John's,  
576 847-852. Balkema, Rotterdam
- 577 McNamara A.M., Goodey R.J. and Taylor, R.N. (2009). Apparatus for centrifuge modelling of top  
578 down basement construction with heave reducing piles. *International Journal of Physical*  
579 *Modelling in Geotechnics*, **9**, No. 1, 1-14. <https://doi: 10.1680/ijpmg.2009.9.1.01>

- 580 Merifield R.S. (2011). Ultimate uplift capacity of multiplate helical type anchors in clay. *J. of*  
581 *Geotechnical and Geoenvironmental Engineering*, **137**, No. 7, 704–716.
- 582 Merifield R.S. and C. C. Smith. (2010). The ultimate uplift capacity of multi-plate strip anchors in  
583 undrained clay. *Computers and Geotechnics*, **37**, No. 4, 504-514.
- 584 Meyerhof G.G. (1951). The ultimate bearing capacity of foundations. *Géotechnique*, **2**, No. 4, 301-  
585 332.
- 586 O'Neill M.W., Hawkins R. A., and Mahar L. (1982). Load transfer mechanisms in piles and pile  
587 groups. *J. Geotech. Engrg. Div.*, **108**, No. 12, 1605–1623.
- 588 Phillips R. (1995). Centrifuge modelling: practical Considerations. In *Geotechnical Centrifuge*  
589 *Technology* (Taylor RN (ed.)). Blackie Academic and Professional, Glasgow, UK, ch. **3**, 34–59.
- 590 Pilcon (2020). Hand vane tester User guide. See [http://www.impact-](http://www.impact-test.co.uk/docs/SL815_HB.pdf)  
591 [test.co.uk/docs/SL815\\_HB.pdf](http://www.impact-test.co.uk/docs/SL815_HB.pdf) . (accessed 02/09/2020)
- 592 Qian J.G., Gao Q., Wang B., Xue J.F., and Huang M.S. (2017): Physical and numerical pull-out  
593 modelling of ribbed piles. *Proceedings of the Institution of Civil Engineers: Geotechnical*  
594 *Engineering*, **170**, No. 1, 51–61.
- 595 Rao S., Prasad Y. and Shetty M. (1991). The behaviour of model screw piles in cohesive soils.  
596 *Soil and Foundations*, **31**, No. 2, 35–50.
- 597 Schofield A.N. and Taylor R.N. (1988). Development of standard geotechnical centrifuge  
598 operations. *Proc. Centrifuge 88, Paris*, 29–32.
- 599 Skempton A.W. (1959). Cast-in-situ bored piles in London clay. *Géotechnique*, **9**, No. 4, 153-173.
- 600 Stallebrass S.E. and Taylor R.N. (1997). The development and evaluation of a constitutive model  
601 for the prediction of ground movements in overconsolidated clay. *Géotechnique*, **47**, No. 2, 235-  
602 253.
- 603 Stanier SA, Black JA, Hird CC (2014) Modelling helical screw piles in soft clay and design  
604 implications. *Proceedings of the Institution of Civil Engineers: Geotechnical Engineering*, **167**, No.  
605 5,447–460.
- 606 Taylor R.N., Rose A.V. and Gorasia R.J. (2013). Pile and Pile Group Capacity: Some Findings  
607 from Centrifuge Tests. *International Journal of Geo-Engineering*, **5**, No. 2, 5-15.
- 608 Watanabe K., Sei H., Nishiyama T and Ishii Y. (2011). Static axial reciprocal load test of cast-in-  
609 place nodular concrete pile and nodular diaphragm wall. *Geotechnical engineering journal of the*  
610 *SEAGS & AGSSEA*, **42**, No. 2.
- 611 Wood D.M. (2004). Geotechnical modelling. New York: Spon Press.
- 612 Zhou J.J., Gong, X.N., Zhang R.H., Hesham El Naggar M. and Wang K.H. (2020). Field behavior  
613 of pre-bored grouted planted nodular pile embedded in deep clayey soil. *Acta Geotechnica*, **15**,  
614 No. 7, 1847-1857. doi:10.1007/s11440-019-00891-x
- 615

616 **Appendix A**

617 In this section the calculations of the bearing capacity of the rib under plain strain and  
 618 axisymmetric conditions are presented.

619 With reference to Figure 13 the components of the internal work are listed in Table 5.

620 The internal work is then:

$$W_{int} = \left( (3\pi + 2) + \frac{h}{b} \cdot \left( \frac{\sqrt{2}}{2} + \left( \frac{2 + \sqrt{2}}{2} \right) \cdot \alpha \right) \right) \cdot \delta \cdot b \cdot s_u \quad (11)$$

621

622 As the pile is a rigid body, the external load can be conveniently applied on the rib length  $b$  instead  
 623 of the pile head. The external work is thus:

624

$$W_{ext} = Q_u \cdot \delta = q_u \cdot b \cdot \delta \quad (12)$$

625

626 Equating eq. (11) and (12) the bearing factor  $N_{c,PL}$  under plane strain conditions is:

627

$$N_{c,PL} = (3\pi + 2) + \frac{h}{b} \cdot \left( \frac{\sqrt{2}}{2} + \left( \frac{2 + \sqrt{2}}{2} \right) \cdot \alpha \right) \quad (13)$$

628

629 For vanishing heights of the rib, the solution converges to the deeply buried single anchor  
 630 mechanism developed by Rowe and reported in Merifield and Smith (2010). For  $\alpha=1$ , the failure  
 631 mechanism is similar to the second mechanism proposed the authors.

632 Under axisymmetric conditions, which apply to a ribbed pile, the surface of revolution around the  
 633 centre line of the pile must be calculated explicitly. This is done by multiplying the work done on  
 634 each interface or fan in the failure mechanism, see Table 5, with the corresponding revolution  
 635 surface:

$$W_{fan1,pile} = W_{fan2,pile} = \delta \cdot b \cdot s_u \cdot \pi \cdot (d + b) \quad (14)$$

636

$$W_{fan1} = W_{fan2} = \frac{3}{2} \pi \cdot \delta \cdot b \cdot s_u \cdot 2\pi \cdot \left( \frac{d}{2} + b \right) \quad (15)$$

637

$$W_1 = \left( \left( \frac{2 + \sqrt{2}}{2} \right) \cdot \alpha \cdot 2\pi \cdot \left( \frac{d}{2} + b \right) + \frac{\sqrt{2}}{2} \cdot 2\pi \cdot \left( \frac{d}{2} + b + \sqrt{2}b \right) \right) \delta \cdot h \cdot s_u \quad (16)$$

638 Hence the internal work is:

639

$$\begin{aligned} W_{int} &= W_{fan1,pile} + W_{fan1} + W_2 + W_{fan2} + W_{fan1,pile} = \\ &= \delta \cdot b \cdot s_u \cdot \pi \left[ 2 \cdot (d + b) + 2 \cdot 3\pi \cdot \left( \frac{d}{2} + b \right) \right. \\ &\quad \left. + \frac{h}{b} \left( \sqrt{2} \cdot \left( \frac{d}{2} + b + \sqrt{2}b \right) + \alpha \cdot \left( \frac{2 + \sqrt{2}}{2} \right) \cdot \left( \frac{d}{2} + b \right) \right) \right] \end{aligned} \quad (17)$$

640 And the external work is:

641

$$W_{ext} = Q_u \cdot \delta = q_u \cdot \pi \cdot \left[ \left( \frac{d}{2} + b \right)^2 - \frac{d^2}{4} \right] \cdot \delta = q_u \cdot \pi \cdot [b^2 + db] \cdot \delta \quad (18)$$

642

643 It is possible to notice that in eq. (17) there is a term that is the bearing factor under plane strain  
644 conditions. Equating eq. (17) to (18) and reducing gives:

645

$$q_u = s_u \cdot \left[ N_{c,PL} + \frac{b}{(b+d)} \cdot \left( 3\pi + \frac{h}{b} \left( \frac{\sqrt{2}}{2} \cdot (1 + 2\sqrt{2}) + \alpha \cdot \left( \frac{2 + \sqrt{2}}{2} \right) \right) \right) \right] \quad (19)$$

646

647 Then, naming A the term inside the round brackets, one could write:

$$\frac{q_u}{s_u} = N_{c,PL} + \frac{b}{(b+d)} \cdot A = N_{c,PL} \cdot \left( 1 + \frac{b}{(b+d)} \cdot \frac{1}{N_{c,PL}} \cdot A \right) \quad (20)$$

648

649 In eq. (19) the ratio  $\frac{q_u}{s_u}$  is the bearing capacity factor  $N_{c,rb}$  while the term inside the brackets is  
650 termed  $\xi$  and is the shape factor that accounts for the axisymmetric conditions. Finally, eq. (20)  
651 assumes the form:

652

$$\frac{q_u}{S_u} = N_{c,rib} = N_{c,PL} \cdot \xi \quad (21)$$

653

654 As shown in Figure 16,  $\xi$  decreases with decreasing  $b/d$  ratios and is practically independent from

655  $\alpha$ . For the model pile tested,  $\xi$  is equal to 1.097.

656

657

Table 1: Mechanical parameters of the Speswhite Kaolin clay.

Parameter	Value
Slope of the critical state line in the $q$ - $p'$ space, $M$	0.89
Specific volume on the critical state line at $p'=1\text{kPa}$ , $\Gamma$	3.04
Slope of the normal compression line in the $v$ - $\ln p'$ space, $\lambda$	0.18
Specific gravity, $G_s$	2.61

658

659

Table 2: Summary of the variables investigated.

<b>Parameter</b>	<b>Value</b>
shape	domed, flat pyramid
active length, $L_a/L$	0.29, 0.67, 0.83, 0.85
vertical spacing, $s/b$	5, 10, 13.3, 20, 40, 80
number of nodules, $n$	2, 4, 8
position, $z/L$	0.21, 0.5, 0.58, 0.77

660

661

Table 3: Main parameters of the response of the plain piles.

<b>Test ID</b>	<b>ultimate capacity, <math>Q_u</math> (N)</b>	<b>dead weight, <math>W</math> (N)</b>	<b>back calculated <math>\alpha</math></b>
T03	350	37.82	0.73
T04	410	37.82	0.79
T05	350*	37.82	0.76
T06	350*	37.82	0.76
T08	400	37.82	0.73
T09	420*	37.82	0.8
T10	430*	37.82	0.78
T12	342*	46.18	0.6
T13	375*	46.18	0.64
T14	375	46.18	0.67

\* values of ultimate capacity that have been estimated

662

Table 4: Main parameters of the response of the impression piles.

Test ID	shape	active length, $L_a$ (mm)	spacing, $s$ (mm)	number of nodules, $n$	position, $z$ (mm)	ultimate capacity, $Q_u$ (N)	capacity increase
T03	dome	152.5	7.5	4	88.75	490	1.4
T04	dome	152.5	7.5	4	88.75	555	1.35
T03	pyramid	152.5	7.5	4	88.75	510	1.46
T04	pyramid	152.5	7.5	4	88.75	569	1.39
	pyramid	152.5	7.5	4	88.75	570	1.39
T05	pyramid	152.5	7.5	4	88.75	490*	1.4
	pyramid	52.5	7.5	4	38.75	425*	1.21
	pyramid	52.5	7.5	4	88.75	410	1.17
T06	pyramid	52.5	7.5	4	138.75	405*	1.16
	pyramid	150	15	4	90	470*	1.34
T08	pyramid	120	15	4	105	490	1.23
	pyramid	120	30	4	105	475*	1.19
	pyramid	120	20	4	105	525	1.31
T09	pyramid	120	30	4	105	518*	1.23
	pyramid	120	20	4	105	515	1.23
	pyramid	120	15	4	105	500	1.19
T10	pyramid	120	20	4	105	550*	1.28
T12	pyramid	120	60	4	105	410*	1.2
	pyramid	120	120	4	105	386*	1.13
T13	pyramid	52.5	7.5	4	38.75	390*	1.04
	pyramid	52.5	7.5	8	38.75	450	1.2
	pyramid	52.5	7.5	2	38.75	387*	1.03
T14	pyramid	52.5	7.5	4	38.75	410	1.09
	pyramid	52.5	7.5	4	38.75	390	1.04

\*values of ultimate capacity that have been estimated

Table 5: Calculation of the internal work on the ribs under plain strain conditions.

Component	Length	Displacement	Strength	Work
fan1,P	$\sqrt{2} \cdot b$	$\frac{\sqrt{2}}{2} \cdot \delta$	$s_u$	$b \cdot \delta \cdot s_u$
fan1	$\frac{3}{4} \pi \cdot \sqrt{2} \cdot b$	$\frac{\sqrt{2}}{2} \cdot \delta$	$s_u$	$2 \cdot \left(\frac{3}{4} \pi \cdot b \cdot \delta \cdot s_u\right)^*$
1,O	$h$	$\frac{\sqrt{2}}{2} \cdot \delta$	$s_u$	$\frac{\sqrt{2}}{2} \cdot h \cdot \delta \cdot s_u$
1,P	$h$	$\left(1 + \frac{\sqrt{2}}{2}\right) \cdot \delta$	$\alpha \cdot s_u$	$\left(\frac{2 + \sqrt{2}}{2}\right) \cdot h \cdot \delta \cdot \alpha \cdot s_u$
fan2	$\frac{3}{4} \pi \cdot \sqrt{2} \cdot b$	$\frac{\sqrt{2}}{2} \cdot \delta$	$s_u$	$2 \cdot \left(\frac{3}{4} \pi \cdot b \cdot \delta \cdot s_u\right)^*$
fan2,P	$\sqrt{2} \cdot b$	$\frac{\sqrt{2}}{2} \cdot \delta$	$s_u$	$b \cdot \delta \cdot s_u$

\*note that the work made by the fan is 2 times the work made by the circular sector.

667 **Figure Captions**

668 Figure 1: Ribbed and impression pile concept.

669 Figure 2. Model geometry.

670 Figure 3: Shape of the nodules.

671 Figure 4: Vertical cross section of the impression tool.

672 Figure 5: Distribution with depth of (a) water content, (b) shear strength from water content, (c)  
673 shear strength from hand vane and (d) OCR at the end of the tests.

674 Figure 6: Load settlement curves for the plain piles.

675 Figure 7: Correlation between the ultimate capacity of the plain piles and average values of  $s_u$   
676 evaluated from water content.

677 Figure 8: Influence of impression parameters on the ultimate capacity: (a) active length  $L_a$ , (b)  
678 normalised variables.

679 Figure 9: Influence of impression parameters on the ultimate capacity: (a) spacing  $s$ , (b)  
680 normalised variables.

681 Figure 10: Influence of impression parameters on the ultimate capacity: (a) number of nodules  $n$ ,  
682 (b) normalised variables.

683 Figure 11: Influence of impression parameters on the ultimate capacity: (a) position along the pile  
684  $z$ , (b) normalised variables.

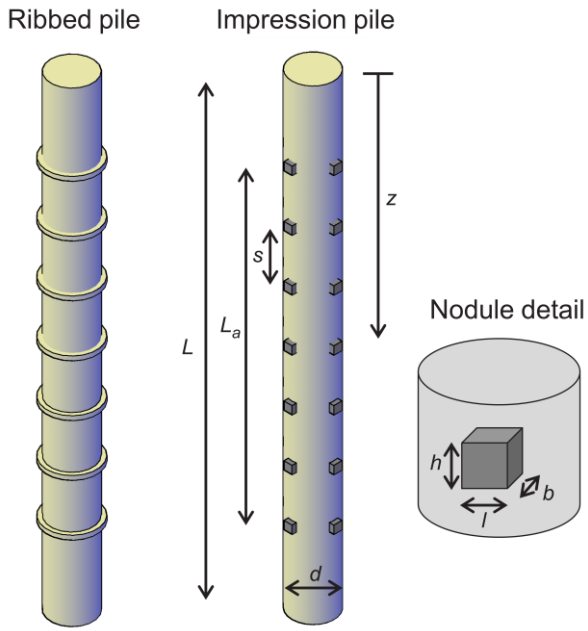
685 Figure 12: Capacity of the impression pile.

686 Figure 13: Failure mechanism of the single rib.

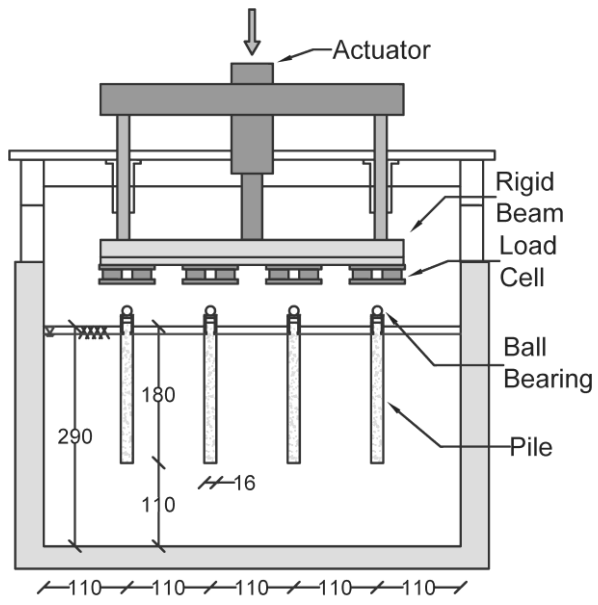
687 Figure 14: Normalised critical spacing.

688 Figure 15: Comparison between measured and calculated ultimate capacity of the impression  
689 piles.

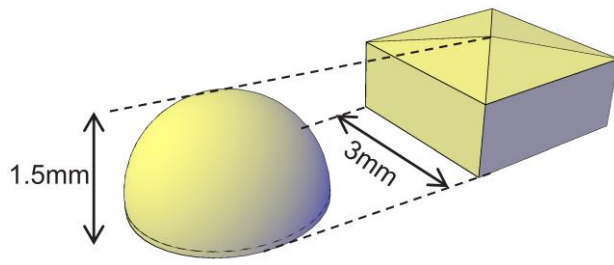
690 Figure 16: Shape factor for the rib failure mechanism.



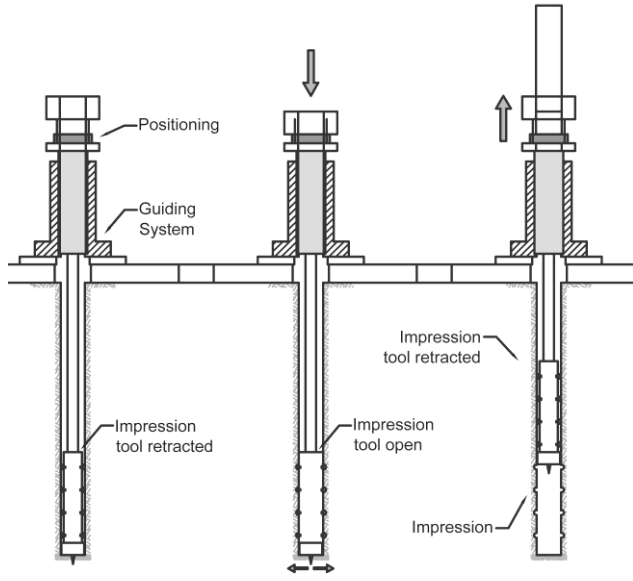
691



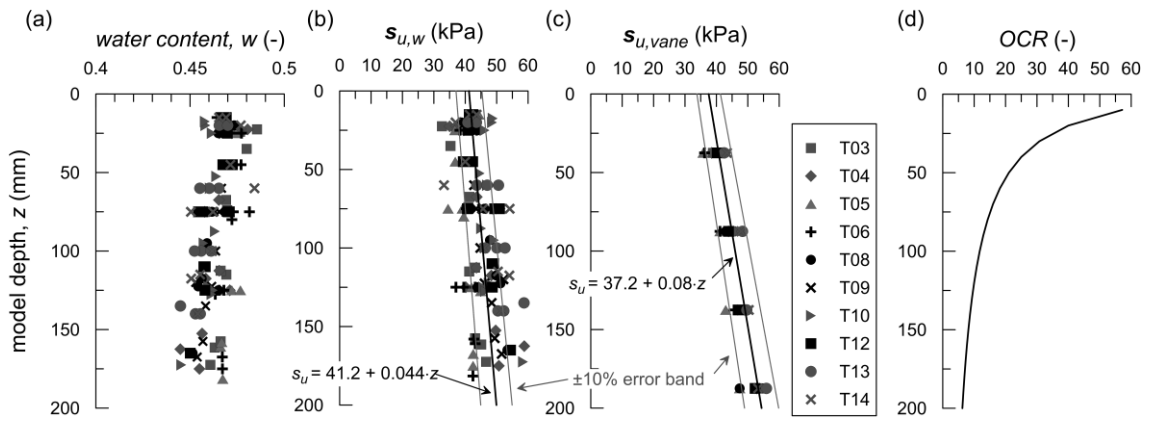
692



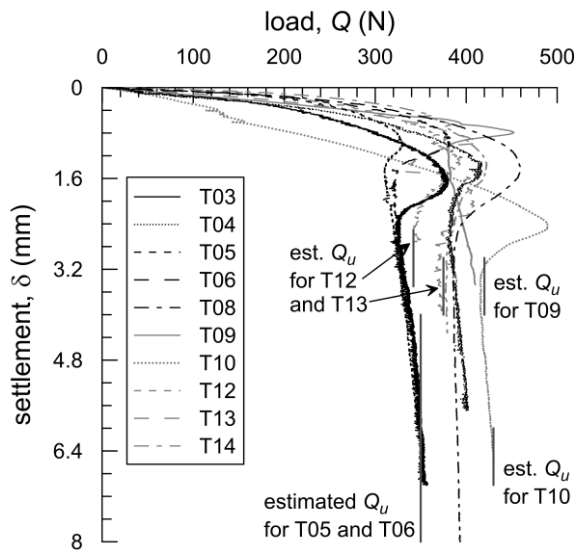
693



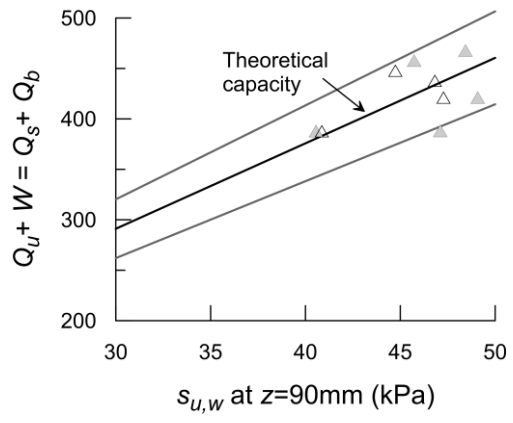
694



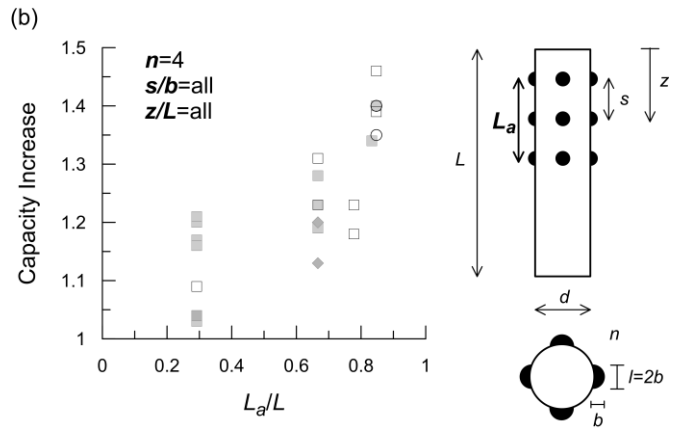
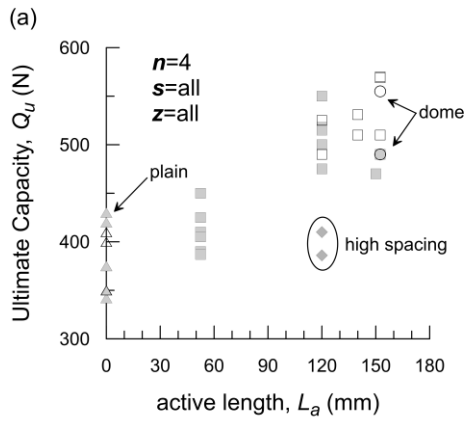
695



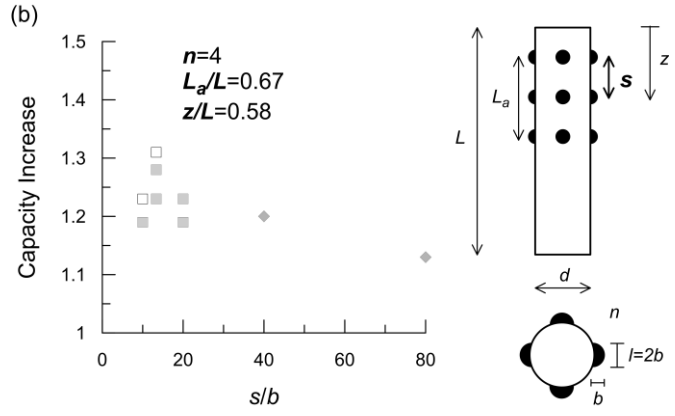
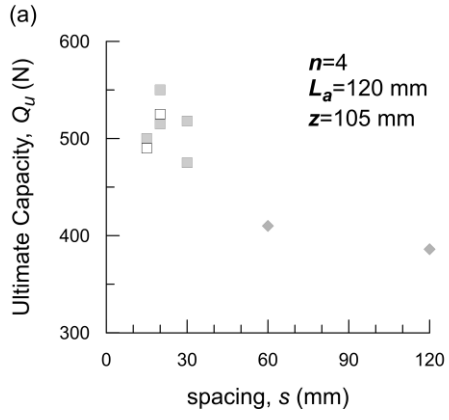
696



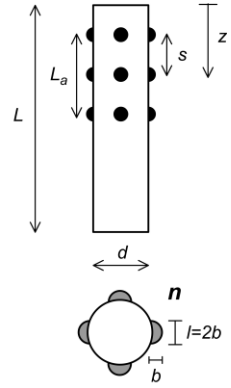
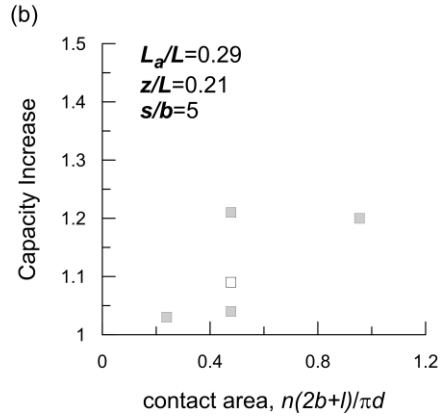
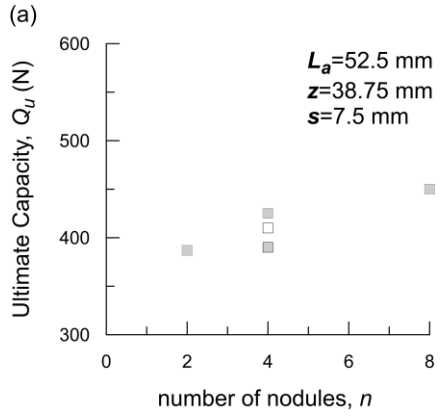
697



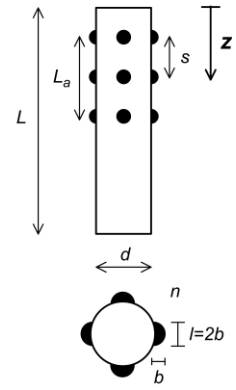
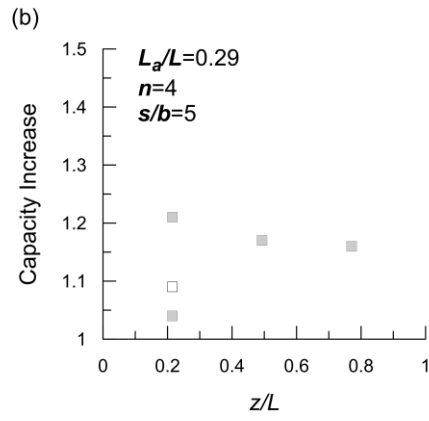
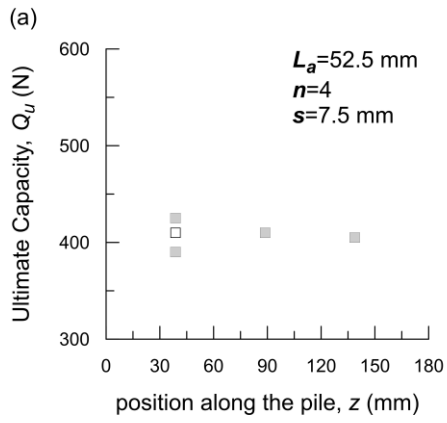
698



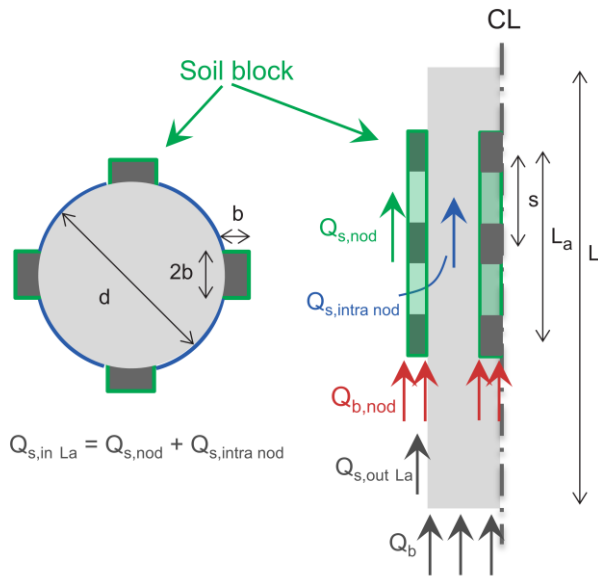
699



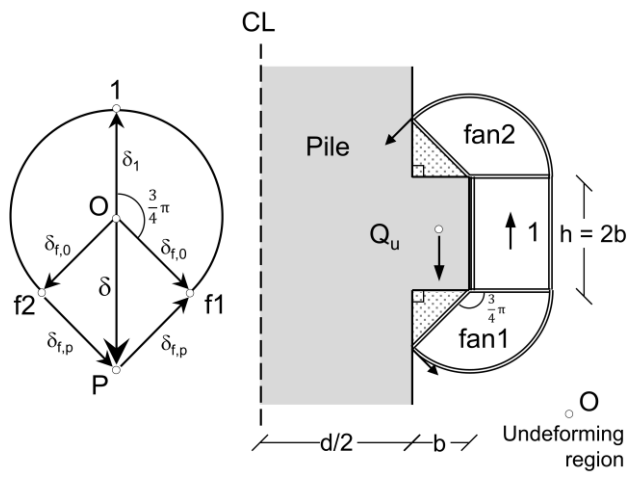
700



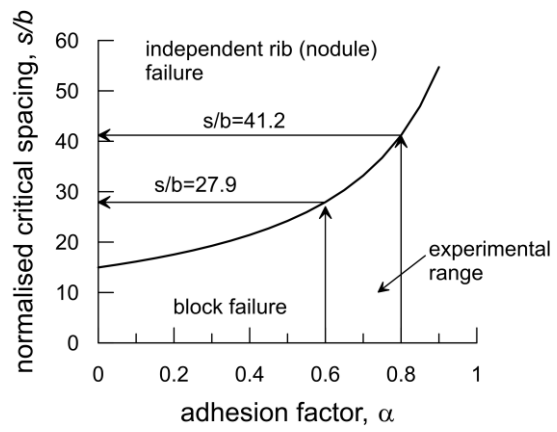
701



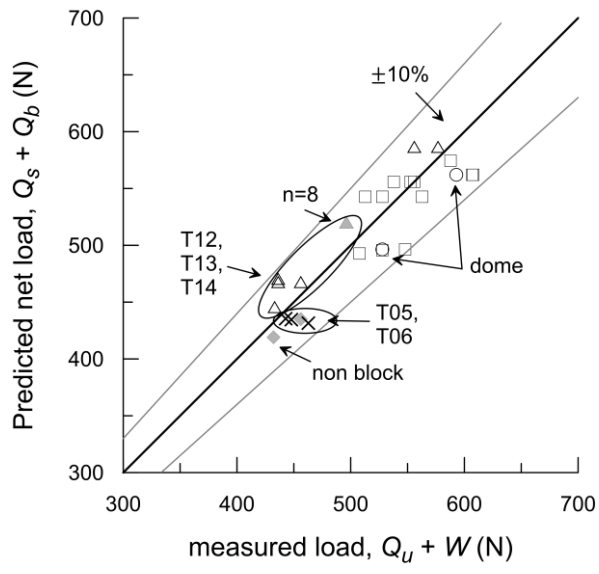
702



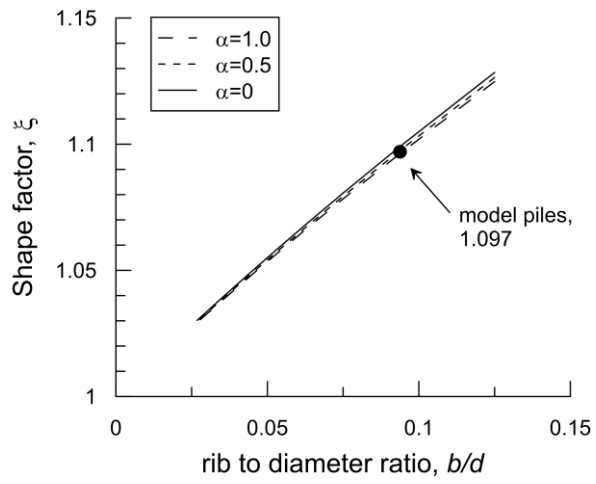
703



704



705



706